ANNALS OF GEOPHYSICS, 67, 6, GP656, 2024; doi:10.4401/ag-9146
OPEN ACCESS

Novel Detectors Based on the Elliott Function for Mapping Potential Field Data: Application to Aeromagnetic Data from Indiana, United States

Ahmad Alvandi[1], Vahid Ebrahimzadeh Ardestani[1], Seyed-Hani Motavalli-Anbaran[*,1]

(1) Institute of Geophysics, University of Tehran, Tehran, Iran

Article history: received August 30, 2024; accepted December 03, 2024

Abstract

One of the primary objectives in interpreting potential field data is to delineate the horizontal boundaries of subsurface geological structures. Several detectors have been developed to achieve this goal by utilizing field-directional gradients. However, these detectors are associated with limitations, such as low resolution, the generation of spurious edges, and dependence on the depth of the causative source. In this study, we introduce two novel detectors that combine gradient amplitude derivatives with the Elliott function (EF) and a modified version of the Elliott function (MEF) to enhance the clarity and precision of boundary identification. The effectiveness of these proposed techniques is demonstrated through the evaluation of synthetic gravity and magnetic datasets, as well as a real case study from the Indiana region in the United States. To mitigate noise in both synthetic and real models, vertical derivatives have been calculated using the β-vertical derivative ratio (β-VDR) technique. Our results indicate that the proposed filters can reduce artifacts in the pseudo-boundary map and produce high-resolution outcomes.

Keywords: Boundary detection; β-VDR technique; Elliott function; Modified Elliott function; Potential field

1. Introduction

Interpreting potential field data offers essential insights into subsurface geological features that are not easily observable through conventional techniques. Compared to other geophysical methods, potential field techniques provide greater cost efficiency and comprehensiveness (Ardestani et al., 2022; Alvandi et al., 2022a; Pham et al., 2024). To identify geological structures, horizontal boundary detection filters are commonly employed to interpret anomalies of potential field data (e.g., Ekinci and Yigitbas, 2015; Pal et al., 2016; Cooper, 2020; Narayan et al., 2021; Deniz Toktay et al., 2021; Eldosouky et al., 2021; Alvandi et al., 2022b; Chen and Zhang, 2022; Pham et al., 2022; Pham and Prasad, 2023; Alvandi and Ardestani, 2023; Pham, 2023; Al-Bahadily et al., 2023; Alvandi et al., 2023; Ai et al., 2024a; Alvandi and Motavalli-Anbaran, 2024; Deniz Toktay et al., 2024). A variety of methods have been developed to delineate these horizontal boundaries, primarily by utilizing first-order and second-order derivatives of the potential field data (Eldosouky et al., 2022; Alvandi and Ardestani, 2023).

The horizontal boundaries were identified by Cordell and Grauch (1985) using the Total Horizontal Derivative (THDR). In the THDR detector, the buried source boundaries of the potential field exhibit the highest values. The THDR can be expressed as follows:

$$\mathrm{THDR} = \sqrt{\left(\frac{\partial \mathrm{T}}{\partial \mathrm{x}}\right)^2 + \left(\frac{\partial \mathrm{T}}{\partial \mathrm{y}}\right)^2} \tag{1}$$

In Eq. (1), $\frac{\partial \mathrm{T}}{\partial \mathrm{x}}$ and $\frac{\partial \mathrm{T}}{\partial \mathrm{y}}$ represent the x- and y-directional derivatives of the reduced-to-the-pole (RTP) magnetic and gravity data.

Roest et al. (1992) mapped the horizontal boundaries of the causative source using the peaks of the analytic signal amplitude (AS). The total gradient is another term for the AS detector, which is defined by utilizing both the vertical and horizontal derivatives of the field (Nabighian, 1984). This can be expressed as follows:

$$\mathrm{AS} = \sqrt{\left(\frac{\partial \mathrm{T}}{\partial \mathrm{x}}\right)^2 + \left(\frac{\partial \mathrm{T}}{\partial \mathrm{y}}\right)^2 + \left(\frac{\partial \mathrm{T}}{\partial \mathrm{z}}\right)^2} \tag{2}$$

In relation (2), $\frac{\partial \mathrm{T}}{\partial \mathrm{z}}$ represents the vertical derivative of the field. One drawback of these detectors is their limited capacity to delineate deep boundaries (Alvandi et al., 2023; Ai et al., 2024a). Additionally, AS is unable to accurately define the edges of thin sources.

Local phase filters, also known as normalized detectors, have been developed to solve this issue. The tilt derivative (TDR), or tilt angle, serves as a local phase detector by normalizing the vertical derivative through the use of horizontal derivatives. The formula for the TDR detector is presented as follows (Miller and Singh, 1994):

$$\mathrm{TDR} = \tan^{-1}\left(\frac{\frac{\partial \mathrm{T}}{\partial \mathrm{z}}}{\sqrt{\left(\frac{\partial \mathrm{T}}{\partial \mathrm{x}}\right)^2 + \left(\frac{\partial \mathrm{T}}{\partial \mathrm{y}}\right)^2}}\right) \tag{3}$$

Although the TDR can detect various anomalies at different depths, it does not generate sharp signals over horizontal boundaries (Eldosouky et al., 2022).

Cooper and Cowan (2006) introduced a revised version of the total horizontal derivative, known as the horizontal tilt derivative (TDX) detector. This detector normalizes the THDR using the vertical gradient and identifies the maxima over the horizontal boundaries of the body. The TDX is expressed as follows:

$$\mathrm{TDX} = \tan^{-1}\left(\frac{\sqrt{\left(\frac{\partial \mathrm{T}}{\partial \mathrm{x}}\right)^2 + \left(\frac{\partial \mathrm{T}}{\partial \mathrm{y}}\right)^2}}{\left|\frac{\partial \mathrm{T}}{\partial \mathrm{z}}\right|}\right) \tag{4}$$

Ferreira et al. (2013) introduced another detector for identifying horizontal boundaries. This detector is known as the tilt derivative of the THDR (TAHG), which can be calculated as follows:

$$\mathrm{TAHG} = \tan^{-1}\left(\frac{\frac{\partial \mathrm{THDR}}{\partial \mathrm{z}}}{\sqrt{\left(\frac{\partial \mathrm{THDR}}{\partial \mathrm{x}}\right)^2 + \left(\frac{\partial \mathrm{THDR}}{\partial \mathrm{y}}\right)^2}}\right) \tag{5}$$

In Eq. (5), $\frac{\partial \mathrm{THDR}}{\partial \mathrm{x}}$, $\frac{\partial \mathrm{THDR}}{\partial \mathrm{y}}$ and $\frac{\partial \mathrm{THDR}}{\partial \mathrm{z}}$ are derivatives of THDR in directions x, y, and z, respectively. The TAHG delineates the boundaries of shallow and deep structures (Alvandi et al., 2023; Ai et al., 2024b). However, the edge resolution of the TAHG map is low (Alvandi and Ardestani, 2023; Ai et al., 2024b).

Based on Ferreira et al. (2013), Oksum et al. (2021) developed an improved detector known as the Fast-Sigmoid Edge Detector (FSED). This detector is computed using the vertical and horizontal derivatives of the THDR and is defined as follows:

$$\mathrm{FSED} = \frac{\mathrm{R}' - 1}{1 + |\mathrm{R}'|} \tag{6}$$

where

$$\mathrm{R}' = \frac{\frac{\partial \mathrm{THDR}}{\partial \mathrm{z}}}{\sqrt{\left(\frac{\partial \mathrm{THDR}}{\partial \mathrm{x}}\right)^2 + \left(\frac{\partial \mathrm{THDR}}{\partial \mathrm{y}}\right)^2}} \tag{7}$$

The FSED peaks indicate the horizontal boundaries in a manner similar to the TAHG detector.

To enhance the resolution of edge detection maps, Ibraheem et al. (2023) introduced a detector that relies on a user-selected parameter (M) to generate sharp signals and improve resolution. This detector is referred to as the impTDX total horizontal derivative. The THDR_impTDX detector can be expressed as follows:

$$\mathrm{THDR\_impTDX} = \sqrt{\left(\frac{\partial \mathrm{impTDX}}{\partial \mathrm{x}}\right)^2 + \left(\frac{\partial \mathrm{impTDX}}{\partial \mathrm{y}}\right)^2} \tag{8}$$

where the impTDX is given by:

$$\mathrm{impTDX} = \tanh\left(\frac{\mathrm{M} \times \left(\frac{\partial^2 \mathrm{T}}{\partial \mathrm{z}^2}\right)}{\sqrt{\left(\frac{\partial \mathrm{TDX}}{\partial \mathrm{x}}\right)^2 + \left(\frac{\partial \mathrm{TDX}}{\partial y}\right)^2}}\right) \tag{9}$$

In Eq. (9), $\frac{\partial \mathrm{TDX}}{\partial \mathrm{x}}$ and $\frac{\partial \mathrm{TDX}}{\partial \mathrm{y}}$ are horizontal derivatives of TDX, $\frac{\partial^2 \mathrm{T}}{\partial \mathrm{z}^2}$ is the vertical derivative of the $\frac{\partial \mathrm{T}}{\partial \mathrm{z}}$, and M is the average value of the gravity and magnetic field.

2. Novel approaches (EF and MEF)

This study presents two advanced detectors with high-resolution capabilities that utilize the Elliott function (Elliott, 1993) and its modified variant (Liu, 2022) to delineate the horizontal boundaries of potential field sources at various depths. The arctangent and hyperbolic tangent functions have been applied to most of the filters introduced in gravity and magnetic data edge enhancement techniques (Alvandi and Ardestani, 2023; Ai et al., 2024a). The Elliott function, which closely resembles the inverse tangent function, is frequently employed to define the horizontal boundaries in gravity and magnetic field data. This approach is exemplified in various methodologies, such as TDR (Miller and Singh, 1994), TDX (Cooper and Cowan, 2006), and TAHG (Ferreira et al., 2013), among others. Building on the work of Oksum et al. (2021), the directional derivatives of THDR are integrated with the Elliott function to introduce a novel detector, referred to as the EF. This detector is formally defined as follows:

$$\mathrm{EF} = \frac{1}{2} + \left(\frac{\frac{\mathrm{R} - \frac{1}{2}}{2}}{\frac{1}{2} + |\mathrm{R}|}\right) \tag{10}$$

where

$$R = \frac{3 \times \frac{\partial THDR}{\partial z}}{\sqrt{\left(\frac{\partial THDR}{\partial x}\right)^2 + \left(\frac{\partial THDR}{\partial y}\right)^2}} - {}^{\pi}/_{4} \tag{11}$$

Additionally, another suggested detector utilizes a revised version of the Elliott function for the THDR derivatives. The modified Elliott function (MEF) detector is expressed as:

$$MEF = \frac{1}{2} + \left(\frac{({}^{R}/_{2})}{\sqrt{1 + R^2}}\right) \tag{12}$$

In Eq. (10), the R-value is calculated using Eq. (11). The primary objective of the proposed detectors is to identify regions that exhibit abrupt changes in density or magnetization. The peaks of the Elliott Function (EF) and the Modified Elliott Function (MEF) delineate the boundaries of anomalous bodies. The amplitude of both the EF and MEF ranges from 0 to 1. A significant advantage of these proposed filters is their ability to accurately and sharply indicate boundaries. Unlike many contemporary high-resolution methods, the resolution of the EF and MEF results does not depend on user-selected parameters (e.g., Pham et al., 2019; Ibraheem et al., 2023; Alvandi and Ardestani, 2023; Alvandi et al., 2023).

3. β-vertical derivative ratio method

This study employs the β-vertical derivative ratio (β-VDR) technique to calculate vertical derivatives ($\frac{\partial T}{\partial z}$, and $\frac{\partial THDR}{\partial z}$), utilizing a novel formula to mitigate the effects of noise (Oliveira and Pham, 2022). Additionally, all horizontal gradients and the total horizontal derivative (THDR) in Eq. (11) are computed in the spatial domain using finite difference method (Ekinci et al., 2020).

$$\frac{\partial THDR}{\partial z} = \frac{b_1 THDR(h_1) + b_2 THDR(h_2) + b_3 THDR(h_3) + b_4 THDR(h_4) + b_5 THDR(h_5)}{\Delta h} \tag{13}$$

where $b_1, \ldots, b_5$ are provided by:

$$\begin{aligned} b_1 &= (2\beta^3 + 15\beta^2 + 35\beta + 25)/12\,. \\ b_2 &= (-8\beta^3 - 54\beta^2 - 104\beta - 48)/12. \\ b_3 &= (12\beta^3 + 72\beta^2 + 114\beta + 36)/12. \\ b_4 &= (-8\beta^3 - 42\beta^2 - 56\beta - 16)/12\,. \\ b_5 &= (2\beta^3 + 9\beta^2 + 11\beta + 3)/12. \end{aligned} \tag{14}$$

Moreover, $THDR(h_i)$ is the data upward-continued to $h_i = d_0 - \beta\Delta h - (i-1)\Delta h$, and d_0 is the observation plane height. In this case, we followed the recommendation of Oliveira and Pham (2022) and used $\beta = 30$ and $\Delta h = 0.1$ of grid spacing. For comprehensive mathematical details and implementation procedures of the β-VDR, refer to Oliveira and Pham (2022).

In the following sections, the effectiveness of the proposed detectors will be evaluated by comparing their results with those obtained from other detectors, including THDR, AS, TDR, TDX, TAHG, FSED, and THDR_impTDX.

4. Application Over the Synthetic Data

4.1 Scenario-1

The effectiveness of the EF and MEF detectors is evaluated using three-dimensional synthetic magnetic and gravity data, both with and without noise. The first scenario examines a model featuring five buried sources, as illustrated in the perspective and plan views in Fig. 1. Table 1 presents a list of the characteristics of the buried prisms. The buried sources were generated using the G&M3D 1.0 package (Wei et al., 2023) at observation points measuring 70 km × 70 km, with a sampling interval of 1 km (Fig. 1c).

Figure 2a illustrates the boundaries detected using the total horizontal derivative (THDR) method applied to the anomaly depicted in Fig. 1c. This figure demonstrates that the large amplitude responses from the shallow sources S4 and S5 dominate the THDR map, while the boundaries of the deeper sources S1, S2, and S3 are characterized by very low resolution. Figure 2b illustrates the analytical signal (AS) detector applied to the gravity anomaly depicted in Fig. 1c. The AS effectively enhances the anomalies associated with the shallow bodies S4 and S5; however, the edges of the deeper sources S1, S2, and S3 appear blurred. Figure 2c presents the TDR map of the gravimetric anomaly depicted in Fig. 1c. The TDR detector does not yield a sharp signal over horizontal boundaries and introduces spurious edge information surrounding source S1. Figure 2d illustrates the edges identified by the horizontal tilt derivative (TDX) detector applied to the gravimetric data in Fig. 1c. This detector produces diffuse borders and does not generate edge information for the deep structure S2. Figure 2e illustrates the boundaries as estimated by the TAHG. This detector is capable of simultaneously mapping edges located at varying depths; however, the resulting edge image exhibits low resolution. Figure 2f illustrates the results of the FSED filter, which effectively delineates the boundaries of

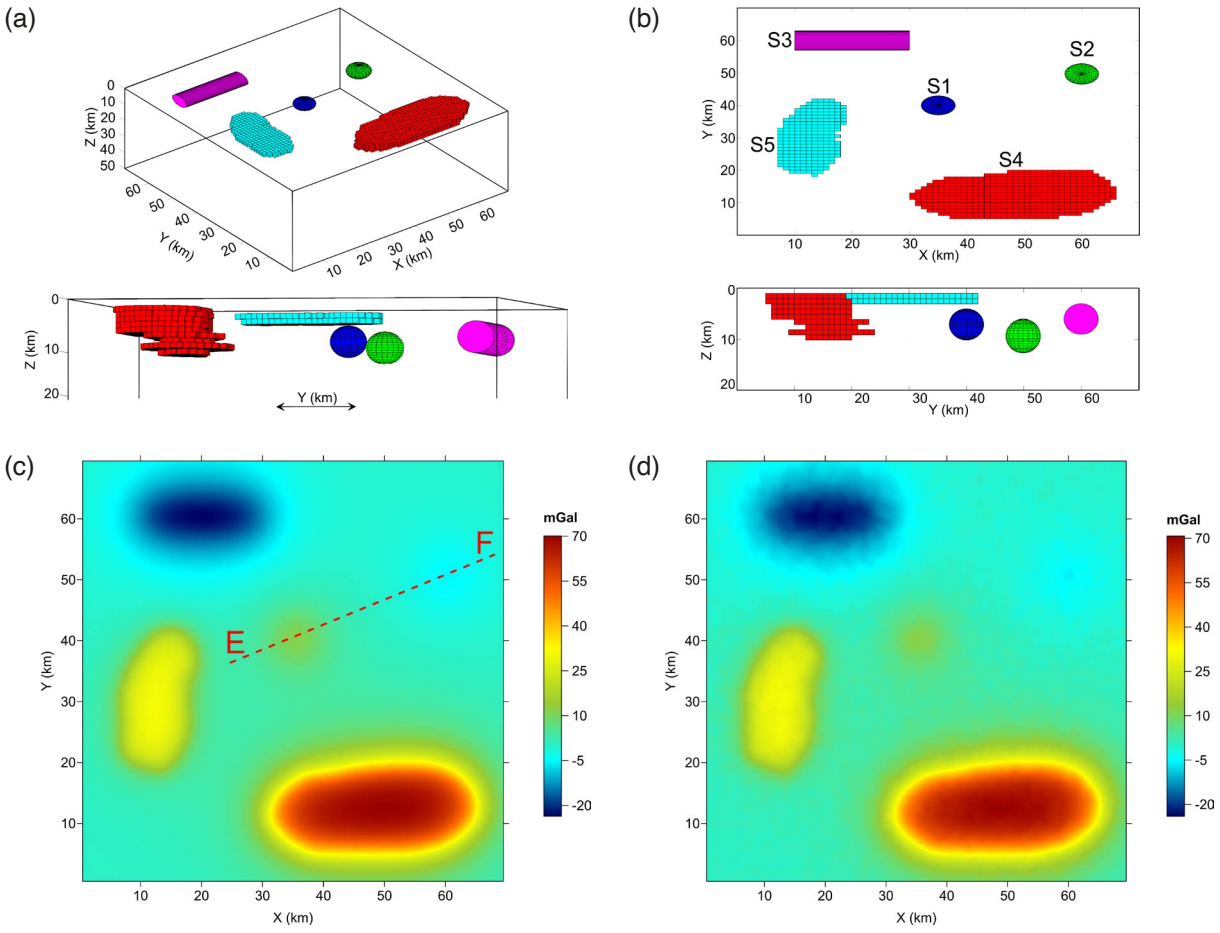

Figure 1. (a) A three-dimensional representation of the gravity model; (b) a plan view; (c) the corresponding gravity anomaly; and (d) a depiction of the noisy gravity anomaly. In (c), the red dashed line represents a profile E-F over the synthetic gravity model.

Parameters/Label	S5 (irregular)	S4 (irregular)	S3 (cylinder)	S2 (sphere)	S1 (sphere)
The center x coordinate (km)	13	49	20	60	35
The center y coordinate (km)	31	14	60	50	40
Depth to the top of the source (km)	1	1	3	6	4
Depth to the bottom of the source (km)	3	10	9	13	10
Density contrast (g/cm^3)	0.4	0.3	−0.5	−0.5	0.4

Table 1. Geometric parameters and designations of the synthetic gravity sources.

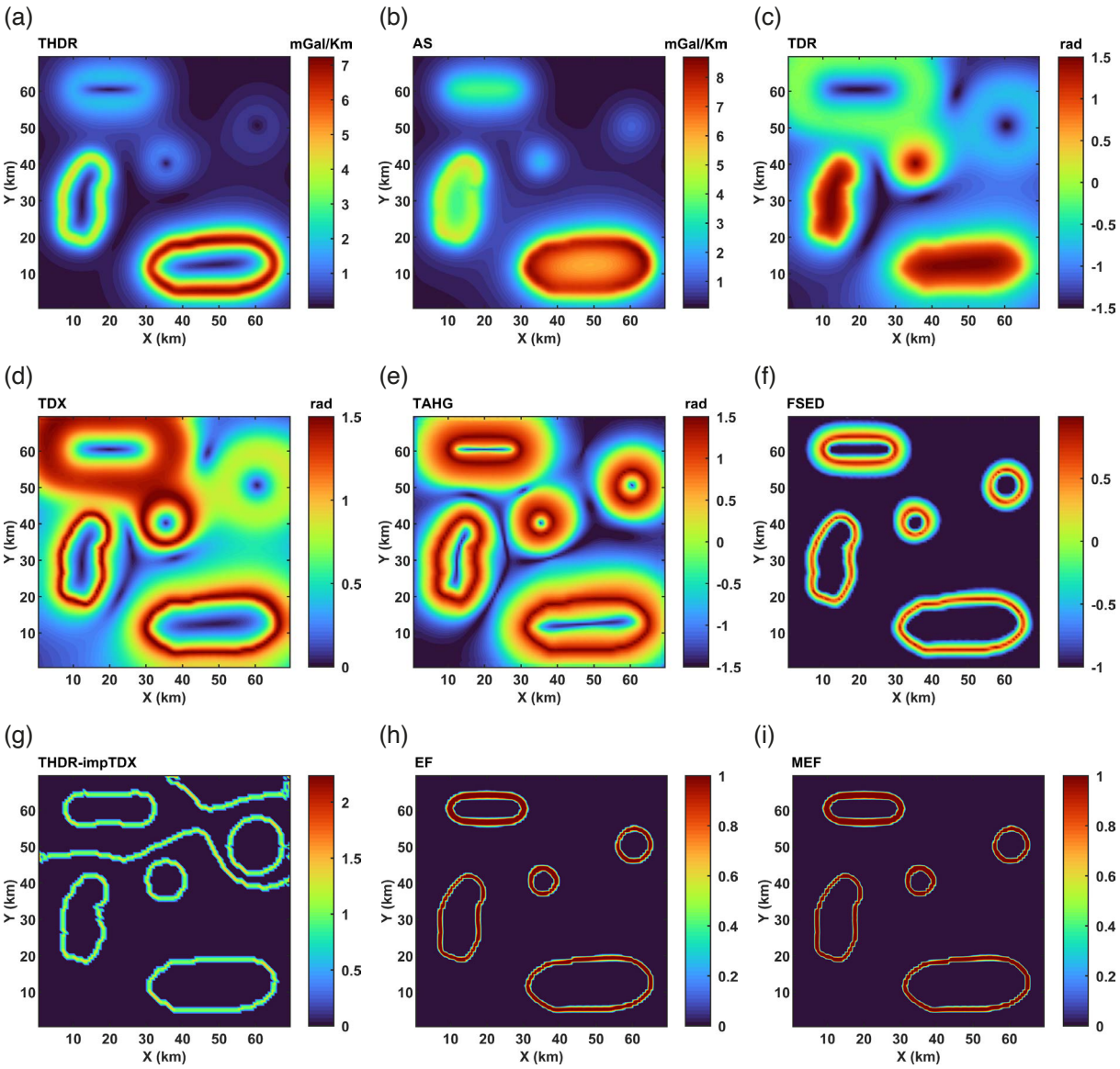

Figure 2. Horizontal boundary determination maps of the data presented in Fig. 2c: (a) THDR, (b) AS, (c) TDR, (d) TDX, (e) TAHG, (f) FSED, (g) THDR_impTDX, (h) EF, and (i) MEF.

the buried structures. Figure 2g illustrates the boundaries calculated using the THDR_impTDX detector, which was applied to the gravimetric data shown in Fig. 1c. The THDR_impTDX offers a high-resolution representation of the edges; however, it also generates false borders around the sources. Figure 2h depicts the boundaries identified by the Elliott function (EF), which locates all sources with high resolution. Figure 2i presents the edges estimated by the modified Elliott function (MEF). Similar to the EF, the MEF produces sharper edges compared to other methods. Unlike THDR_impTDX, the proposed detectors can accurately map all body boundaries without introducing artificial edges.

4.2 Scenario-2

In order to enhance the clarity of the method's efficacy, a two-dimensional cross-section was created, as depicted in Fig. 3. The gravity data along the profile E-F is illustrated in Fig. 3a, while Figs. 3b to 3j present various representations, including THDR, AS, TDR, TDX, TAHG, FSED, THDR_impTDX, EF, and MEF. Notably, EF and MEF demonstrate high resolution in mapping all edges compared to other methods, and the proposed detectors do not delineate false boundaries between and around the buried bodies.

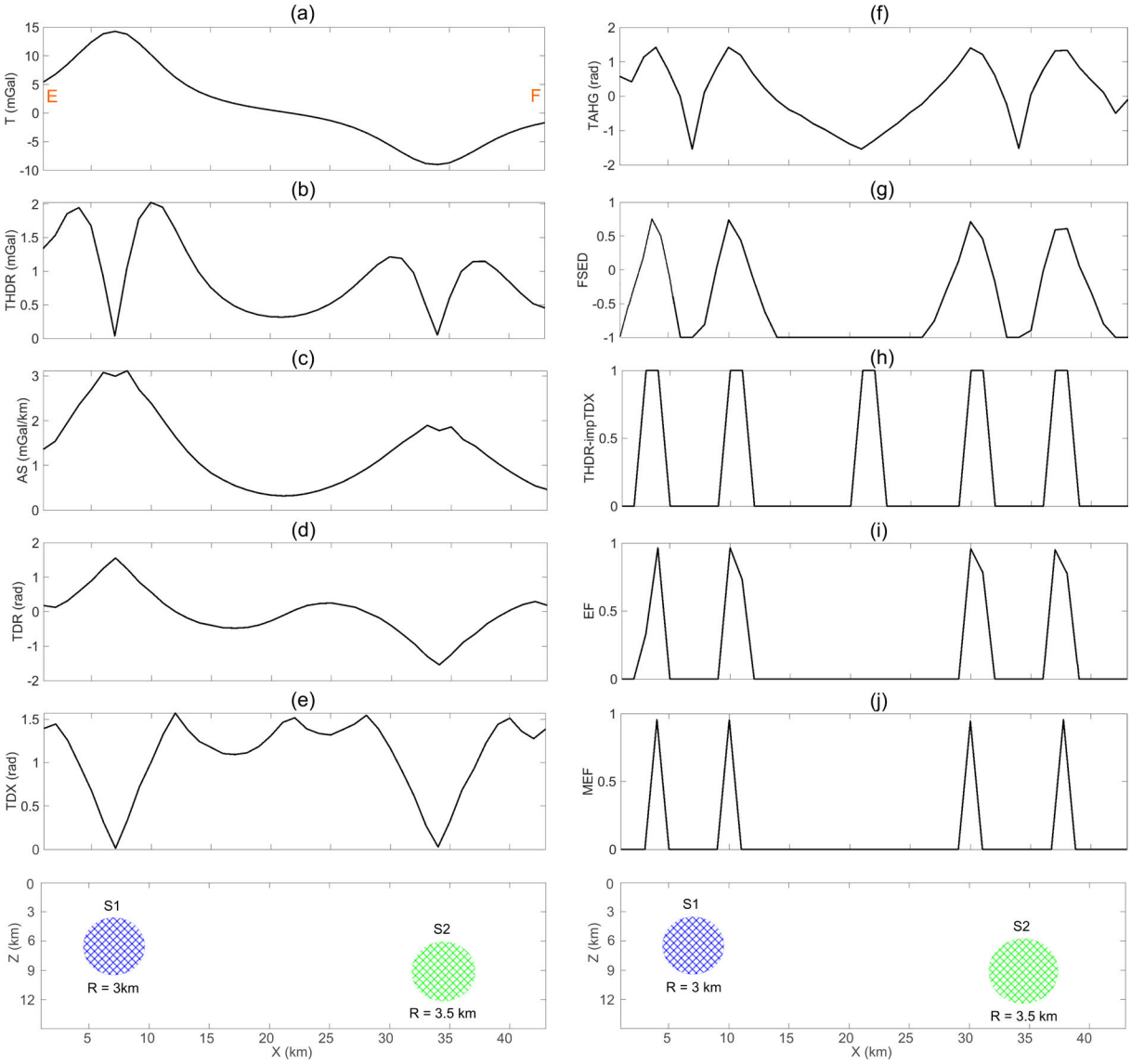

Figure 3. 2-D cross section (Fig. 1c) constructed from the model, (a) gravity anomaly, (b) THDR, (c) AS, (d) TDR, (e) TDX, (f) TAHG, (g) FSED, (h) THDR_impTDX, (i) EF and (j) MEF.

4.3 Scenario-3

To probe the accuracy of the proposed filters, we considered the third scenario where Gaussian noise with standard deviation of 2 mGal was added to the gravity anomaly (Fig. 1d). Figures 4a through 4i display the boundaries established by various detectors, including THDR, AS, TDR, TDX, TAHG, FSED, THDR_impTDX, EF, and MEF, respectively. The THDR detector, which relies solely on horizontal gradients, demonstrates lower sensitivity to noisy data compared to other detectors. However, it remains significantly affected by the deep anomalies associated with structures S1, S2, and S3 (Fig. 4a). Figure 4b illustrates the edges identified by applying the AS to the anomaly depicted in Fig. 1d. This analysis reveals that the large amplitude responses from the shallow sources S3 and S4 dominate the AS map, while the boundaries of the deeper sources S1, S2, and S3 exhibit significantly lower resolution. The sensitivity of this filter is slightly higher than that of the THDR, attributable to the incorporation of the vertical derivative. Figures 4c and 4d illustrate anomalies calculated using the TDR and TDX detectors, respectively. Although both detectors produce balanced images for all sources, they also introduce artifacts around source S1. Figure 4e illustrates the edges extracted using the TAHG method, which produces well-defined boundaries for buried sources. However, the horizontal boundaries in the TAHG map appear diffuse. Figure 4f depicts the anomalies calculated by the Fast-Sigmoid Enhanced Detector (FSED), which utilizes a fast-sigmoid function and THDR gradients, thereby

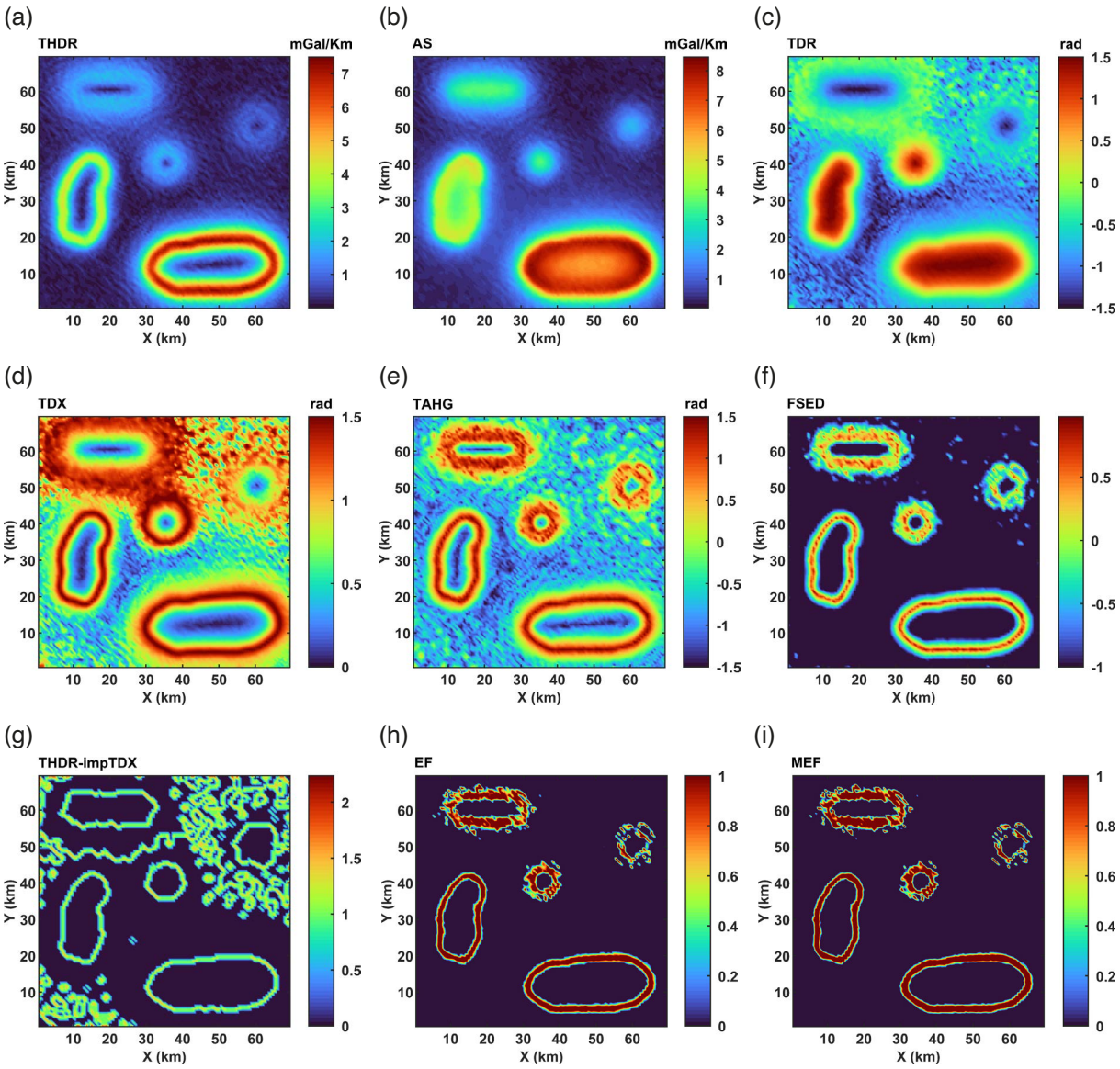

Figure 4. Horizontal boundaries determination maps of data in Fig. 2d: (a) THDR, (b) AS, (c) TDR, (d) TDX, (e) TAHG, (f) FSED, (g) THDR_impTDX, (h) EF, and (i) MEF.

enhancing its effectiveness compared to other detectors. Figure 4g illustrates the edges extracted by the THDR_impTDX detector. The sensitivity of THDR_impTDX surpasses that of other filters due to the incorporation of the second vertical derivative in its calculations. Although this detector is effective in generating well-balanced images from the source edges, the boundaries in the THDR_impTDX map appear diffuse, and the map contains numerous false edges. Figures 4h and 4i illustrate the edges detected by the proposed EF and MEF detectors, respectively. Notably, both EF and MEF effectively identify all edges, even in the presence of noise, without generating false edges around or above the sources. In this context, both EF and MEF produce high-resolution edge images.

4.4 Scenario-4

In the fourth scenario, we evaluate the performance of the developed detectors using the magnetic data obtained from the Bishop model. This dataset is frequently utilized by researchers to assess edge enhancement techniques for complex buried structures (Florio, 2018; Chen and Zhang, 2022; Alvandi and Ardestani, 2023; Al-Bahadily et al., 2023; Ai et al., 2024b). The synthetic data derived from the Bishop model, which is freely available on the SEG website (https://wiki.seg.org/wiki/Bishop_Model), serves as a basis for assessing the effectiveness of the proposed detectors. This evaluation includes a comparative analysis with established detectors, such as THDR, AS, TDR, TDX, TAHG, FSED, and THDR_impTDX. Figure 5a depicts the depth of the model in relation to the volcanic basement, whereas Figs. 5b and 5c display the magnetic anomaly associated with the Bishop model, both in the absence and presence of noise.

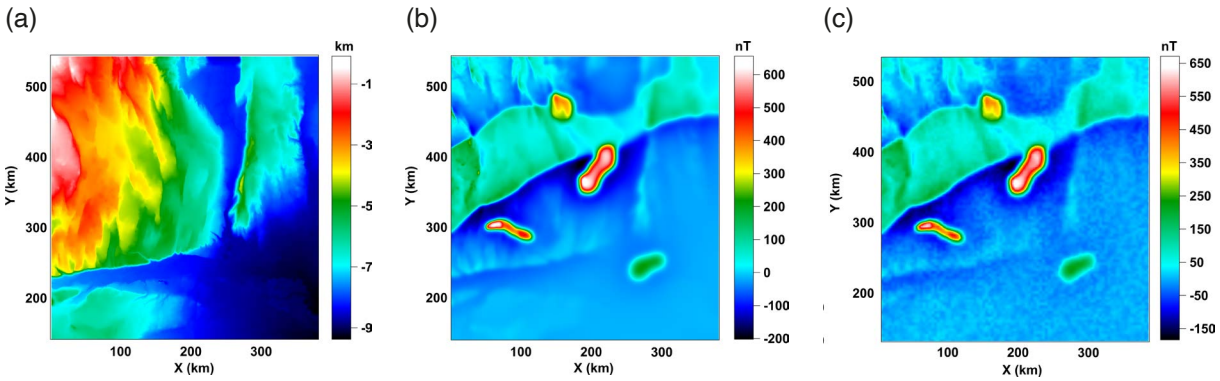

Figure 5. The bishop model includes: (a) basement relief depth, (b) magnetic anomaly, and (c) noisy magnetic anomaly.

Figures 6a and 6b illustrate the results obtained from the THDR and AS methods, respectively. The data indicate that signals emanating from shallow sources primarily influence the outcomes of both techniques, while the delineation of boundaries associated with deeper sources remains unclear. Figure 6c presents the boundary map generated by the TDR method, which is characterized by its absence of sharp edges. Figure 6d illustrates the constraints identified through the application of the TDX detector to the magnetic data shown in Fig. 5b. While this method is effective in mapping all source boundaries, it often generates ambiguous information regarding the boundaries between sources, leading to unclear boundary representations. Figure 6e illustrates the boundaries identified by the TAHG detector, which can simultaneously map boundaries at various depths. However, despite its advanced capabilities, the edge images generated by the TAHG have low resolution. Figure 6f illustrates the boundaries determined by FSED, which can effectively map boundaries at various depths simultaneously. Figure 6g illustrates the limits established by the THDR_impTDX detector as applied to the magnetic data presented in Fig. 5b. This figure demonstrates that while THDR_impTDX offers a high-resolution representation of boundaries, it also introduces false boundaries both between and around the sources. Figure 6h illustrates the contours detected by the EF method. The EF method, similar to the THDR_impTDX and FSED methods, generates higher resolution boundaries compared to those obtained by the THDR, AS, TDR, TDX, and TAHG detectors. However, in contrast to the THDR_impTDX method, the EF method successfully delineates all body boundaries without introducing false edges. Finally, Fig. 6i displays the boundaries detected by the MEF method, which also maps all high-resolution boundaries, similar to the EF method.

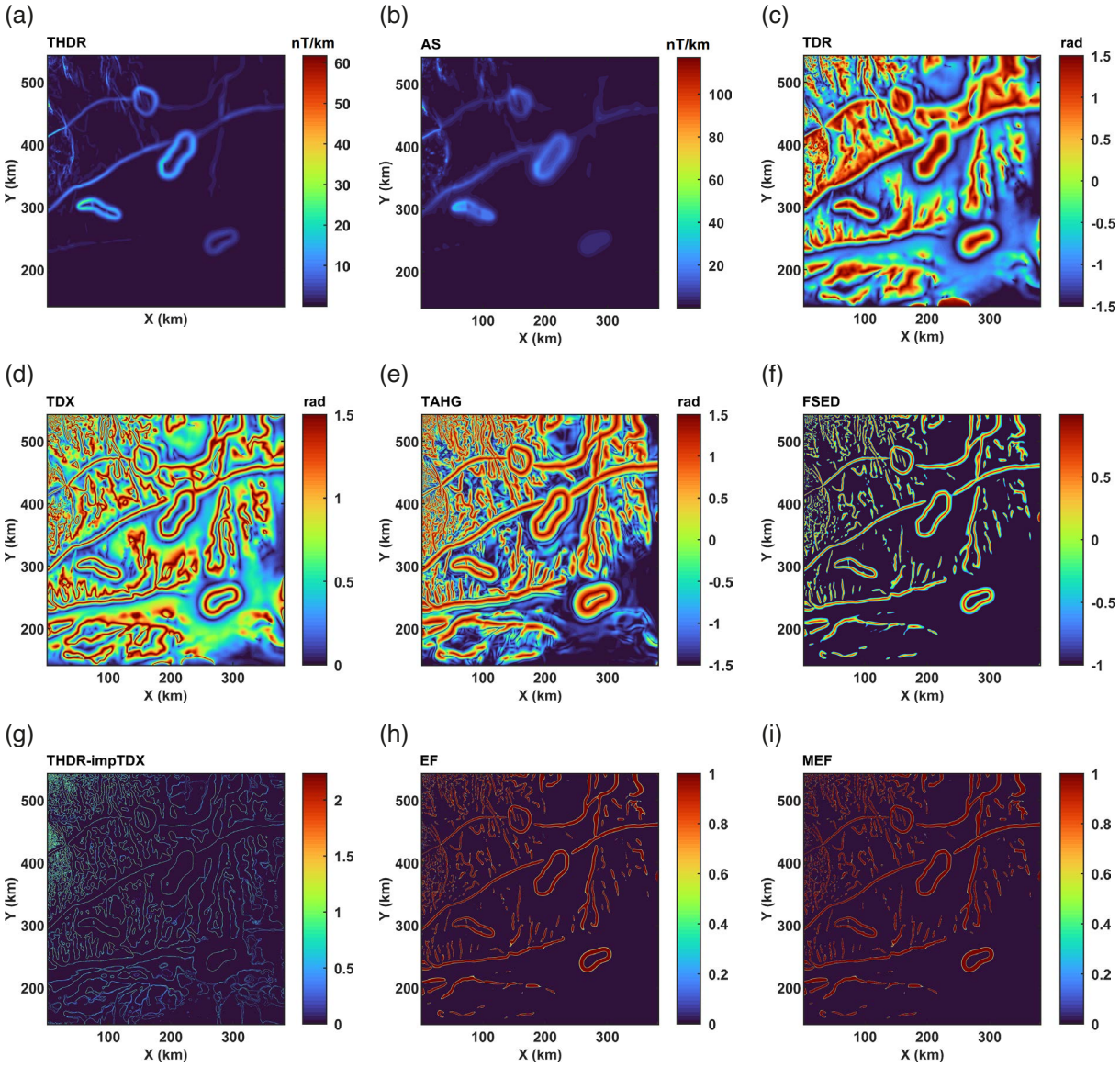

Figure 6. Horizontal boundary determination maps of the data presented in Fig. 5b: (a) THDR, (b) AS, (c) TDR, (d) TDX, (e) TAHG, (f) FSED, (g) THDR_impTDX, (h) EF, and (i) MEF.

4.5 Scenario-5

In the fifth scenario, a study was carried out to evaluate how sensitive the proposed detectors and other detectors are to noise. The observed noise is characterized as Gaussian, with a standard deviation of 3 nT, as illustrated in Fig. 5c. The defined boundaries obtained from the THDR and AS detectors are illustrated in Figs. 7a and 7b, respectively. The THDR detector utilizes horizontal gradients of magnetic data, offering enhanced noise resistance compared to the AS detector, as demonstrated by Saibi et al. (2019). Nevertheless, both detectors are once again characterized by predominant signals originating from shallow sources. In this instance, the TDR and TDX accurately differentiate the margins and create false edges between the origins (Figs. 7c and d). Figure 7e illustrates the boundaries identified by the TAHG detector. This filter is effective in accurately defining everybody's contour while avoiding the creation of false boundaries. However, the contours present within the TAHG map display diffuse edges. Figure 7f illustrates the outcomes of the FSED filter. This filter effectively equalizes different signals from different sources; however, in this case, some edges are faint. Figure 7g illustrates the limits obtained using the THDR_impTDX method. The data indicate that the THDR_impTDX technique is more sensitive to noise than other methods. The THDR_impTDX detector operates by using the second vertical derivative of the magnetic data. Figures 7h and 7i illustrate the edges detected using the EF and MEF methods introduced in this research. The proposed detectors

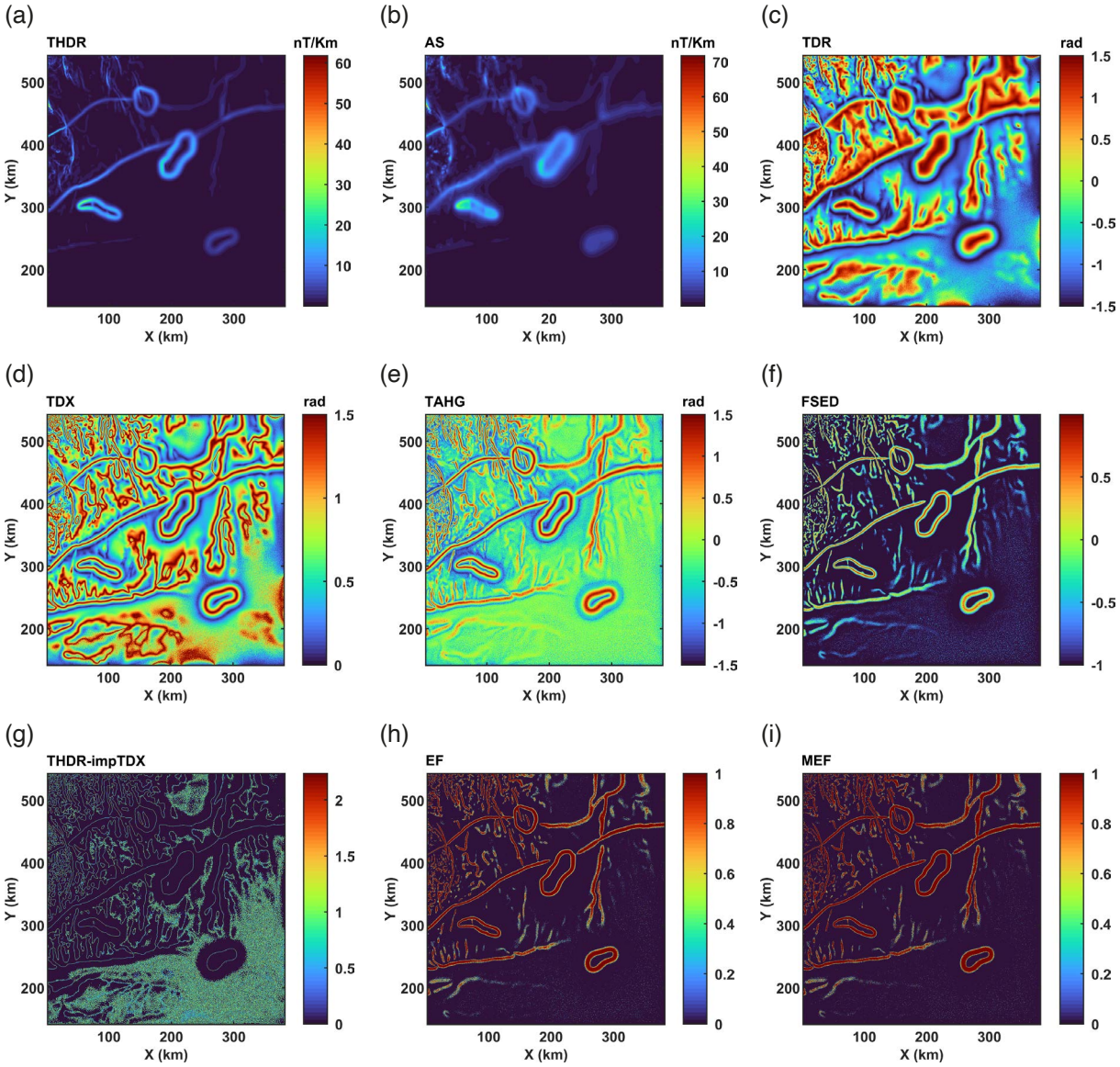

Figure 7. Horizontal boundary determination maps of the data presented in Fig. 5c: (a) THDR, (b) AS, (c) TDR, (d) TDX, (e) TAHG, (f) FSED, (g) THDR_impTDX, (h) EF, and (i) MEF.

effectively identify all edges, even in the presence of noise, without generating false edges around or above the sources. In this context, both the EF and MEF methods produce high-resolution edge images.

5. Application to Aeromagnetic Data

This section evaluates the effectiveness of the proposed filters through the analysis of aeromagnetic data from the Indiana region in the United States. Figure 8 illustrates the geological map of the Indiana area, which features Paleozoic-aged sequences of shale, limestone, and sandstone that exhibit a gentle eastward dip. These geological formations resulted from the accumulation of materials during periods of rising sea levels that inundated extensive portions of the North American continent (Haase et al., 2010). The bedrock units are overlain by unconsolidated deposits formed from multiple glaciation events during the Tertiary and Quaternary periods. Indiana's bedrock has been subject to erosion since the late Pennsylvanian period, approximately 300 million years ago. Over the past 2 million years, the region has been covered by unconsolidated materials due to two major glacial advances and retreats. Bedrock exposure is limited to the south-central region of the state, which remained unglaciated, and specific areas adjacent to the Wabash River (Erd and Greenberg, 1960; Huizing and Russell, 1986).

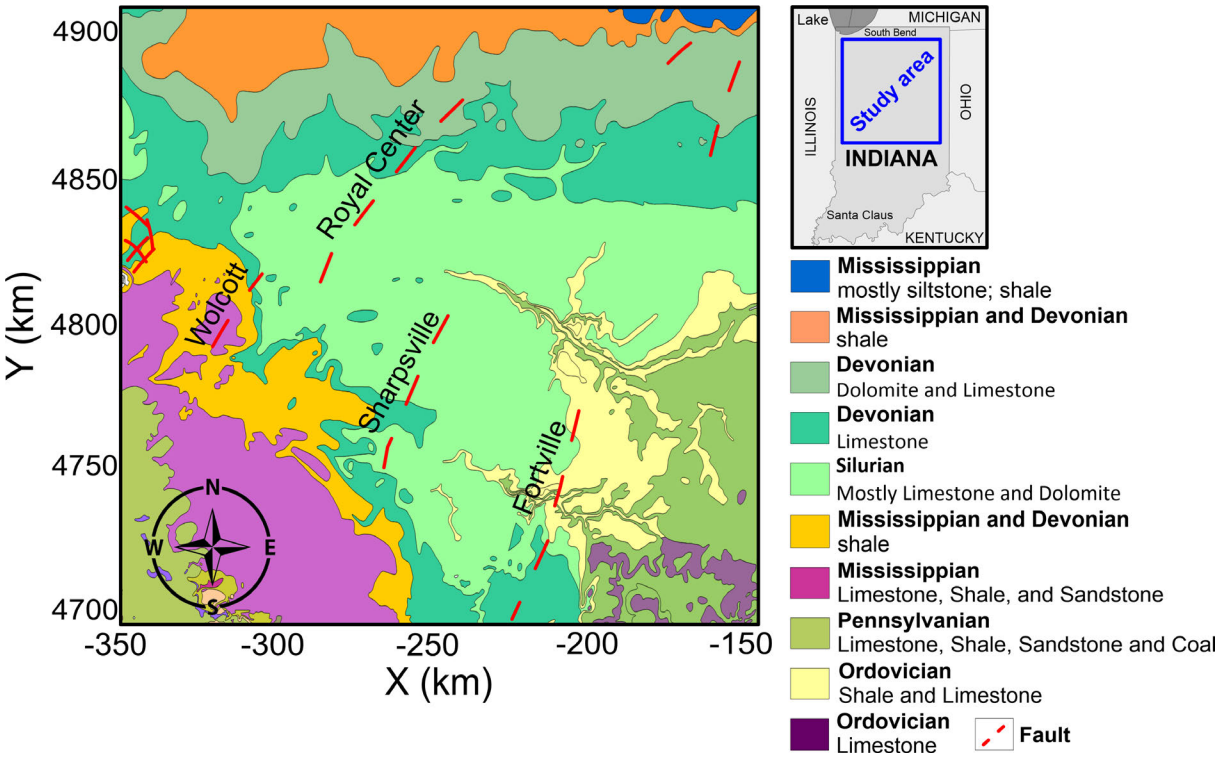

Figure 8. Geological map of the study region with an overlay of the most essential tectonic features adapted (from Gray et al., 1987; Gray, 1989).

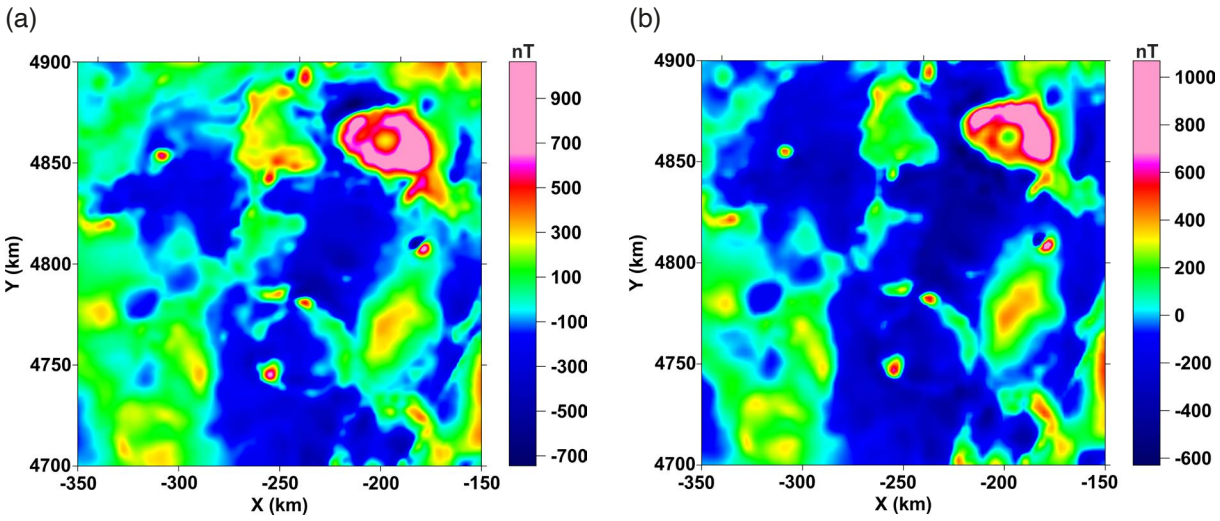

Figure 9. (a) Aeromagnetic data; (b) Reduced-to-the-pole aeromagnetic data for Indiana.

The interpretation of magnetic data is crucial for mineral exploration and geological mapping studies. The magnetic anomaly data for the Indiana region in the United States were developed using grids that integrate magnetic data collected by the United States Geological Survey (USGS) between 1947 and 1994 from 19 distinct magnetic surveys (Henderson and Zietz, 1958; Philbin et al., 1965). The magnetic anomaly maps were digitized along flight lines, which is considered the most accurate method for recovering the original data. All surveys were conducted at an altitude of approximately 300 meters above the ground. The final magnetic anomaly grid, with a 500-meter interval, and a section of the magnetic anomaly map are utilized in the present study and are depicted in Fig. 9a. In interpreting magnetic data, it is essential to first reduce the magnetic anomalies to the pole (RTP) due

to the influence of the magnetization direction (Pei et al., 2020). The RTP aeromagnetic anomaly, obtained using Inclination = 65° and Declination = −4° is displayed in Fig. 9b.

Figures 10a and 10b illustrate the total horizontal derivative (THDR) and analytical signal (AS) maps of the aeromagnetic anomaly identified in the reduced-to-pole (RTP) dataset. The figures illustrate that the total horizontal derivatives and the analytical signal exhibit large amplitude anomalies, which hinder the creation of an accurate structural map of Indiana. Figure 10c illustrates the edge image generated by the TDR detector. This method offers a balanced representation of magnetic sources; however, it produces edges with low resolution. Figure 10d illustrates the results of the TDX detector. Although this detector is more efficient than the THDR, AS, and TDR in producing clear edge images, the edges of the sources appear interconnected. Figure 10e presents the image map obtained through the application of the TAHG algorithm. It is evident that the TAHG method can accurately identify the source edges; however, the edges of the structures are not clearly defined, resulting in a low-resolution image, as noted by Alvandi and Ardestani (2023). Figure 10f illustrates the results of the FSED filter, which effectively balances various signals from various sources. However, in this example, the boundaries of the buried sources are not defined by the maximum amplitude of the FSED. The boundaries delineated by the THDR_impTDX are illustrated in Fig. 10g. Although this detector is capable of producing high-resolution structural images compared to other filters, it is known to introduce false edges above and around the sources. Figures 10h and 10i illustrate the edges identified by the EF and MEF. The EF and MEF demonstrate high-resolution edge detection when compared to alternative techniques, without generating false edges.

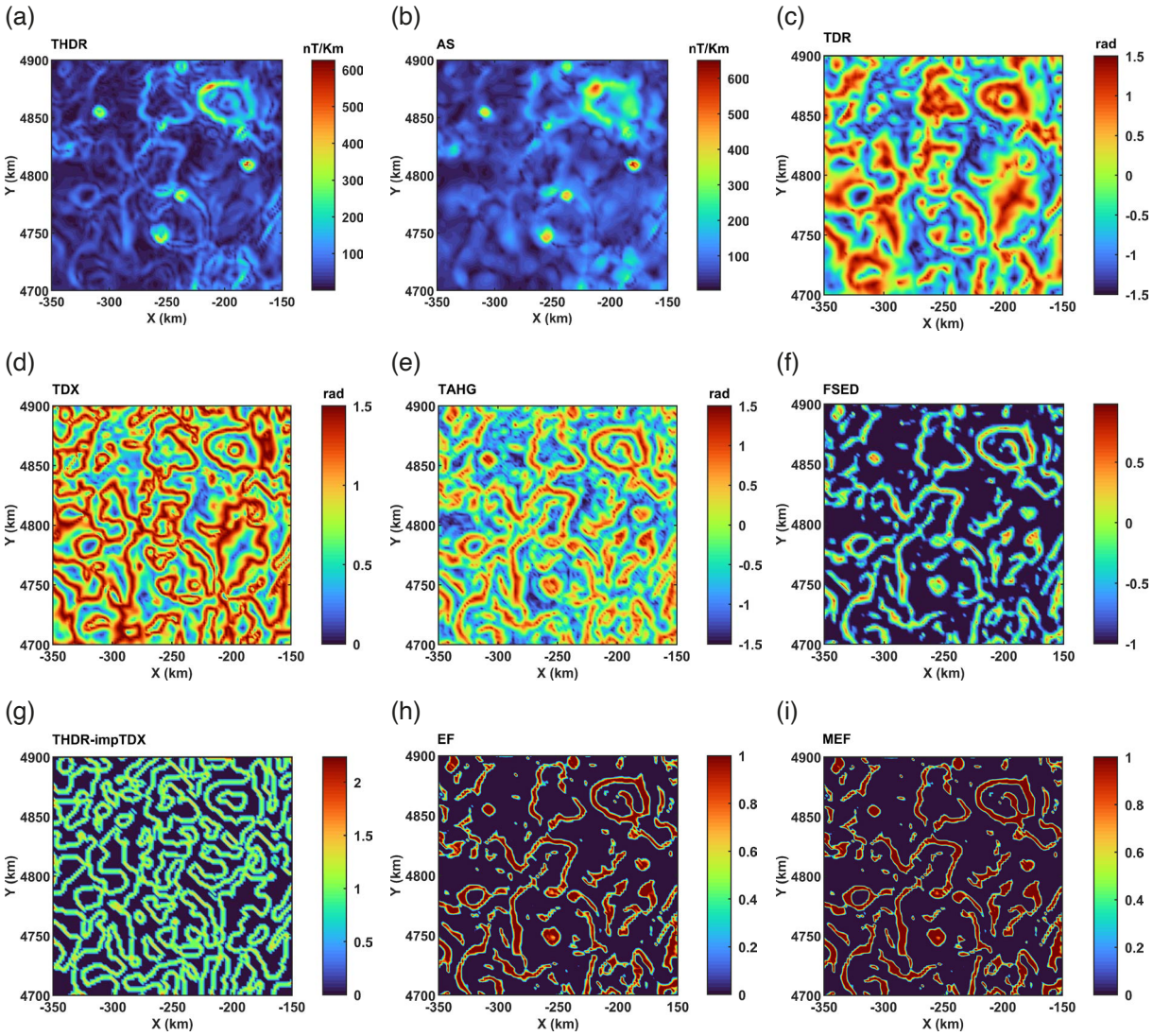

Figure 10. Horizontal boundary determination maps of the data presented in Fig. 9b: (a) THDR, (b) AS, (c) TDR, (d) TDX, (e) TAHG, (f) FSED, (g) THDR_impTDX, (h) EF, and (i) MEF.

6. Conclusions

The identification of horizontal boundaries is crucial for the accurate interpretation of subsurface structures. The precision of this process is significantly improved through noise reduction, which has led to the increased use of innovative filtering techniques. Edge enhancement filters, which detect anomalies through derivatives, have gained prominence despite their tendency to amplify noise within the dataset. However, the Elliott Function (EF) and Modified Elliott Function (MEF) filters, when used in conjunction with vertical derivatives computed through the β-vertical derivative ratio (β-VDR) method, demonstrate superior performance in enhancing both weak and strong signals without introducing extraneous information into the edge map. The application of the EF and MEF filters has notably resulted in the creation of a distinct structural map for a specific region in Indiana, providing valuable insights for the development of a novel structural and tectonic framework. These filters are characterized by their high resolution, ability to eliminate false edges, and capacity to reveal subtle geological features.

Data availability. The datasets generated during and/or analysed during the current work are available from the corresponding author upon reasonable request.

Acknowledgments. We thank the anonymous reviewers for their guidance and constructive comments, which have greatly enhanced the quality of the paper. We also appreciate the United States Geological Survey for granting permission to use the geologic map and aeromagnetic data in Figures 8 and 9a. The data were accessed from https://www.usgs.gov on May 20, 2024.

References

Ai, H., H. Deniz Toktay, A. Alvandi, R. Pasteka et al. (2024a). Advancing potential field data analysis: the Modified Horizontal Gradient Amplitude method (MHGA), Contrib. Geophys. Geod., 54, 2, 119-143, doi:10.31577/congeo.2024.54.2.1.

Ai, H., Y. L. Ekinci, A. Alvandi, H. Deniz Toktay et al. (2024b). Detecting edges of geologic sources from gravity or magnetic anomalies through a novel algorithm based on hyperbolic tangent function, Turk. J. Earth Sci., 33, 6, 6, doi:10.55730/1300-0985.1936.

Al-Bahadily, H. A., A. M. Al-Rahim and R. S. Smith (2023). Determination of reactivated regions and faults in the Iraq Southern Desert with the new edge technique, Inverse Tilt Angle of Second-gradients (ITAS), Acta Geophys., 72, 1675-1692, doi:10.1007/s11600-023-01176-4.

Alvandi, A. and V. E. Ardestani (2023). Edge detection of potential field anomalies using the Gompertz function as a high-resolution edge enhancement filter, B. Geophys. Oceanogr., 64, 279-300, doi:10.4430/bgo00420.

Alvandi, A. and S. H. Motavalli-Anbaran (2024). Detection of the horizontal boundary of gravity anomalies using the hybrid positive and negative curvature (PNH) procedure, J. Earth Space Phys., 50, 2, 323-340, doi:10.22059/jesphys.2024.362046.1007541.

Alvandi, A., K. Su, H. Ai, V. E. Ardestani et al. (2023). Enhancement of potential field source boundaries using the hyperbolic domain (Gudermannian Function), Minerals, 13, 1312, doi:10.3390/min13101312.

Alvandi, A., H. Deniz Toktay and S. Nasri (2022a). Application of direct source parameter imaging (direct local wave number) technique to the 2D gravity anomalies for depth determination of some geological structures, Acta Geophys., 70, 659-667, doi:10.1007/s11600-022-00750-6.

Alvandi, A., H. Deniz Toktay and L. T. Pham (2022b). Capability of improved Logistics filter in determining lateral boundaries and edges of gravity and magnetic anomalies Tuzgolu Area, Turkey, Min. Eng., 17, 56, 57-72, doi:10.22034/ijme.2022.538984.1889.

Ardestani, V. E., D. Fournier and D. W. Oldenburg (2022). A localized gravity modeling of the upper crust beneath central Zagros, Pure Appl. Geophys., 179, 6-7, 2365-2381, doi:10.1007/s00024-022-03065-1.

Chen, T. and G. Zhang (2022). NHF as an edge detector of potential field data and its application in the Yili Basin, Minerals, 12, 149, doi:10.3390/min12020149.

Cooper, G. R. J. (2020). A modified enhanced horizontal derivative filter for potential field data, Explor. Geophys., 51, 549-554, doi:10.1080/08123985.2020.1725386.

Cooper, G. R. J. and D. R. Cowan (2006). Enhancing potential field data using filters based on the local phase, Comput. Geosci., 32, 1585-1591, doi:10.1016/j.cageo.2006.02.016.

Cordell, L. and V. J. S. Grauch (1985). Mapping basement magnetization zones from aeromagnetic data in the San Juan Basin, New Mexico, in The Utility of Regional Gravity and Magnetic Maps W. J. Hinze (Ed.), Society of Exploration Geophysicists, 181-197, doi:10.1190/1.0931830346.ch16.

Castro, F., S. Oliveira, J. D. Souza and F. Ferreira (2018). GRAV-MAG SUITE: An open source MATLAB-based program for processing potential field data, in Proceedings of the VIII Simpósio Brasileiro de Geofísica, doi:10.22564/8simbgf2018.067.

Deniz Toktay, H., K. N. D. Prasad and A. Alvandi (2024). Edge enhancement of potential field data using the enhanced gradient (EG) filter, Bull. Miner. Res. Explor., 174, 55-66, doi:10.19111/bulletinofmre.1386653.

Deniz Toktay, H., D. Aydogan and F. Yüksel (2021). Quantitative analysis of total magnetic anomaly maps on archaeological sites – Part 1, Math. Method. Appl. Sci., 44, 13696-13710, doi:10.1002/mma.7652.

Ekinci, Y. L. and E. Yigitbas (2015). Interpretation of gravity anomalies to delineate some structural features of the Biga and Gelibolu peninsulas and their surroundings (northwest Turkey), Geodinam. Acta, 27, 4, 300-319, doi:10.1080/09853111.2015.1046354.

Ekinci, Y. L., A. Buyuksarac, O. Bektas and C. Ertekin (2020). Geophysical investigation of Mount Nemrut Stratovolcano (Bitlis, Eastern Turkey) through aeromagnetic anomaly analyses, Pure Appl. Geophys., 177, 7, 3243-3264, doi:10.1007/s00024-020-02432-0.

Eldosouky, A. M., R. El-Qassas, A. B. Pour, H. Mohamed et al. (2021). Integration of ASTER satellite imagery and 3D inversion of aeromagnetic data for deep mineral exploration, Adv. Space Res., 68, 9, 3641-3662, doi:10.1016/j.asr.2021.07.016.

Eldosouky, A. M., L. T. Pham and A. Henaish (2022). High precision structural mapping using edge filters of potential field and remote sensing data: a case study from Wadi Umm Ghalqa area, South Eastern Desert, Egypt, Egypt J. Remote Sens. Space Sci., 25, 2, 501-513, doi:10.1016/j.ejrs.2022.03.001.

Elliott, D. L. (1993). A Better Activation Function for Artificial Neural Networks, in ISR Technical Report TR 93-8, Institute for Systems Research, College Park, MD, USA.

Erd, R. C. and S. S. Greenberg (1960). Minerals of Indiana, Indiana Geological Survey Bulletin, 18, 73.

Ferreira, F. J. F., J. de Souza, A. B. S. Bongiolo and L. G. de Castro (2013). Enhancement of the total horizontal gradient of magnetic anomalies using the tilt angle, Geophysics, 78, 3, J33-J41, doi:10.1190/geo2011-0441.1.

Florio, G. (2018). Mapping the depth to basement by iterative rescaling of gravity or magnetic data, J. Geophys. Res. Solid Earth, 123, 10, 9101-9120, doi:10.1029/2018JB015667.

Gray, H. H. (1989). Quaternary Geologic Map of Indiana, Indiana Geological Survey Miscellaneous Map 49, scale 1:500.000, Bloomington, Indiana, USA.

Gray, H. H., C. H. Ault and S. J. Keller (1987). Bedrock Geologic Map of Indiana, Indiana Geological Survey Miscellaneous Map 48, scale 1:500.000, Bloomington, Indiana, USA.

Haase, S. H., C. H. Park, R. L. Nowack and J. R. Hill (2010). Probabilistic Seismic Hazard Estimates Incorporating Site Effects-An Example from Indiana USA, Environ. Eng. Geosci., 16, 4, 369-388, doi:10.2113/gseegeosci.16.4.369.

Henderson, J. R. and I. Zietz (1958). Interpretation of an aeromagnetic survey of Indiana, US Geol. Surv. Prof. Pap., 316-B, 19-37, doi:10.3133/pp316B.

Huizing, T. E. and R. E. Russell (1986). Indiana Minerals: A locality index, Rocks and Minerals, 61, 3, 136-151.

Ibraheem, I., B. Tezkan, H. Ghazala and A. A. Othman (2023). A new edge enhancement filter for the interpretation of magnetic Field Data, Pure Appl. Geophys., 180, 2223-2240, doi:10.1007/s00024-023-03249-3.

Liu, X. (2022). Identification of Encrypted Traffic Using Advanced Mathematical Modeling and Computational Intelligence, Math. Probl. Eng., 1-10, doi:10.1155/2022/1419804.

Miller, H. G. and V. Singh (1994). Potential field tilt a new concept for location of potential field sources, J. Appl. Geophys., 32, 2-3, 213-217, doi:10.1016/0926-9851(94)90022-1.

Nabighian, M. N. (1984). Towards a three-dimensional automatic interpretation of potential field data via generalized Hilbert Transforms-Fundamental relations, Geophysics, 49, 780-786, doi:10.1190/1.1441706.

Narayan, S. U. K., S. K. Pal and S. D. Sahoo (2021). New insights into the structural and tectonic settings of the Bay of Bengal using high-resolution earth gravity model data, Acta Geophys., 69, 2011-2033, doi:10.1007/s11600-021-00657-8.

Oksum, E., D. Le, M. Vu, N. Hang et al. (2021). A novel approach based on the fast sigmoid function for interpretation of potential field data, Boll. Geofis. Teor. Appl., 62, 543-556, doi:10.4430/bgta0348.

Oliveira, S. P. and L. T. Pham (2022). A stable finite difference method based on upward continuation to evaluate vertical derivatives of potential field data, Pure Appl. Geophys., 179, 12, 4555-4566, doi:10.1007/s00024-022-03164-z.

Pal, S. K., T. J. Majumdar, V. K. Pathak, S. Narayan et al. (2016). Utilization of high-resolution EGM2008 gravity data for geological exploration over the Singhbhum-Orissa Craton, India, Geocarto. Int., 31, 7, 783-802, doi:10.1080/10106049.2015.1076064.

Pei, Y., C. Liu and R. Lou (2020). Multi-Scale Edge Detection Method for Potential Field Data Based on Two-Dimensional Variation Mode Decomposition and Mathematical Morphology, IEEE Access, 8, 161138-161156, doi:10.1109/ACCESS.2020.3021287.

Pham, L. T., E. Oksum, T. D. Do, M. Le-Huy et al. (2019). LAS: a combination of the analytic signal amplitude and the generalized logistic function as a novel edge enhancement of magnetic data, Contrib. Geophys. Geod., 49, 4, 425-440, doi:10.2478/congeo-2019-0022.

Pham, L. T., E. Oksum, O. Kafadar, P. T. Trinh et al. (2022). Determination of subsurface lineaments in the Hoang Sa islands using enhanced methods of gravity total horizontal gradient, Vietnam J. Earth Sci., 44, 3, 395-409, doi:10.15625/2615-9783/17013.

Pham, L. T. and K. N. D. Prasad (2023). Analysis of gravity data for extracting structural features of the northern region of the Central Indian Ridge, Vietnam J. Earth Sci., 45, 2, 147-163, doi:10.15625/2615-9783/18206.

Pham, L. T. (2023). A novel approach for enhancing potential fields: application to aeromagnetic data of the Tuangiao, Vietnam, Eur. Phys. J. Plus., 138, 1134, doi:10.1140/epjp/s13360-023-04760-1.

Pham, L. T., S. P. Oliveira, M. Le Huy, D. V. Nguyen et al. (2024). Reliable Euler deconvolution solutions of gravity data throughout the β-VDR and THGED methods: Application to mineral exploration and geological structural mapping, Vietnam J. Earth Sci., 46, 3, 432-448, doi:10.15625/2615-9783/21009.

Philbin, P. W., C. L. Long and F. C. Moore (1965). Aeromagnetic map of the Columbus-Dayton area, Ohio and Indiana, in Geophysical Investigations Map, GP-491, scale 1:250,000, U.S. Geological Survey, USA, doi:10.3133/gp491.

Roest, W. R., J. Verhoef and M. Pilkington (1992). Magnetic interpretation using the 3-D analytic signal, Geophysics, 57, 1, 116-125, doi:10.1190/1.1443174.

Saibi, H., G. Amir and F. S. Mohamed (2019). Subsurface structural mapping using gravity data of AlAin region, Abu Dhabi Emirate, United Arab Emirates, Geophys. J. Int., 216, 2, 1201-1213, doi:10.1093/gji/ggy489.

Wei, K., B. Chen and J. Peng (2023). G&M3D 1.0: An Interactive framework for 3D Model Construction and Forward Calculation of Potential Fields, Geosci. Model Dev. Discuss., preprint, doi:10.5194/gmd-2022-314.

***CORRESPONDING AUTHOR: Seyed-Hani MOTAVALLI-ANBARAN**,
Institute of Geophysics, University of Tehran, Tehran, Iran
e-mail: motavalli@ut.ac.ir